Specialty Journal of Pharmacognosy, Phytochemistry, and Biotechnology
ISSN: 3062-441X
2024, Volume 4, Page No: 221-238

Available online at: www.galaxypub.co/page/journals

Galaxy Publication

Galaxy Publication

A Shared Monocyte-Derived Four-Gene Signature Predicts Prognosis in Cancer and Acute Myocardial Infarction: A Multi-Omics Approach

Artem Shevchenko[1]*, Olexii Bondarenko[1], Serhii Melnyk[1], Dmytro Koval[1]

[1]Department of Natural Products Chemistry, Faculty of Pharmacy, Bogomolets National Medical University, Kyiv, Ukraine.

***E-mail** ✉ artem.shevchenko.np@gmail.com

Received: 21 September 2024; **Revised:** 04 December 2024; **Accepted:** 06 December 2024

ABSTRACT

Patients with cancer encounter a heightened short-term likelihood of cardiovascular complications, whereas individuals suffering an acute myocardial infarction (AMI) tend to show an increased rate of cancer diagnoses. With clinical resources often limited, pinpointing overlapping biomarkers provides a practical and economical strategy for risk evaluation, reducing the need for numerous independent diagnostic procedures. Consequently, recognizing biomarkers that simultaneously relate to cancer survival and AMI risk is essential. Our research indicates that monocyte-associated markers—WEE1, PYHIN1, SEC61A2, and HAL—may function as useful indicators for both cancer prognosis and AMI. Using an innovative computational formula, we assessed mRNA expression patterns in samples from patients with AMI and cancer, which allowed us to construct a new expression-based risk index. When participants were separated into high- and low-risk categories using the median score, Kaplan–Meier curves revealed clearly worse survival for the high-risk subsets in cancer datasets. Additionally, calibration plots, decision curve analysis (DCA), and clinical impact curves further supported the strong diagnostic performance of this risk model for AMI. A notable finding was the mutual activation of the Notch signaling cascade, offering insight into shared high-risk features underlying both diseases. We also confirmed consistent expression differences of these genes in cell lines and clinical tissues, reinforcing their value as candidate biomarkers. Overall, our work highlights the potential of mRNA-based indicators and underscores the importance of continued validation and methodological refinement.

Keywords: Signature, AMI, Cancer, Machine learning, Prognosis

How to Cite This Article: Shevchenko A, Bondarenko O, Melnyk S, Koval D. A Shared Monocyte-Derived Four-Gene Signature Predicts Prognosis in Cancer and Acute Myocardial Infarction: A Multi-Omics Approach. Spec J Pharmacogn Phytochem Biotechnol. 2024;4:221-38. https://doi.org/10.51847/RuMj0Y7Ey0

Introduction

Acute myocardial infarction (AMI) and cancer remain major causes of illness and death worldwide [1]. Although the connection between them is not extensively documented, existing studies reveal that cancer patients carry a greater short-term probability of cardiovascular issues, and individuals who have experienced AMI show an increased likelihood of subsequently developing cancer [2, 3]. These findings imply the existence of underlying biological links between cancer survival and AMI development. Thus, detecting biomarkers that influence both outcomes is critically important.

The elevated cardiovascular vulnerability observed among cancer patients continues to draw significant attention. Evidence demonstrates that survivors of cancer present with higher rates of myocardial infarction, heart failure, and arrhythmias compared to the general public [4]. This heightened risk is believed to stem from multiple causes, including treatment-related cardiac toxicity and overlapping risk determinants shared by both cancer and cardiovascular disorders [5]. Processes such as inflammation, oxidative stress, and endothelial dysfunction—common to both disease categories—may promote cardiac complications in oncology populations [6]. Therefore,

uncovering markers capable of predicting both cancer outcomes and AMI risk may prove valuable for early identification of vulnerable patients during cancer therapy.

Conversely, several investigations also show that AMI is followed by increased rates of malignancies, including lung, colorectal, and hematological cancers [3]. Given the possibility of a bidirectional association, it becomes essential to investigate shared biomarkers that could support earlier diagnosis and improved treatment strategies for both conditions. Advances in molecular profiling, particularly transcriptomics, have made it feasible to reveal gene-expression signatures relevant to both cancer and AMI [7]. Transcriptomic analysis provides a comprehensive overview of differentially expressed genes [8–10], and the integration of multi-omics—combining transcriptomics with genomic and proteomic platforms [11]—offers an even stronger foundation for deciphering the mechanisms linking these diseases.

In our investigation, ovarian cancer (OC) samples were used to evaluate shared diagnostic and prognostic indicators for AMI, an approach that may initially appear unconventional. Nonetheless, OC and AMI share several risk contributors, including obesity, diabetes, and smoking [12, 13], which can predispose individuals to both disorders. By selecting OC samples as an illustrative example, we sought to determine whether common molecular mechanisms or biomarkers [14] associated with these shared pathways contribute to the pathogenesis of both OC and AMI.

We applied a newly designed formula to quantify mRNA expression in clinical AMI and OC specimens. This computation generated a novel risk score derived from these expression patterns. The resulting index effectively predicted AMI likelihood and provided prognostic insight for OC patients. Most importantly, the outcomes highlight that the shared biomarkers—WEE1, PYHIN1, SEC61A2, and HAL—may serve as meaningful predictors in both cancer and AMI settings.

Materials and Methods

Pre-processing of bulk transcriptome data

For the AMI analyses, we re-evaluated two GPL6244-based datasets: GSE59867, which includes 111 AMI and 46 stable CAD subjects at the time of hospital entry, and GSE62646, containing 28 AMI and 14 CAD admissions [15]. The OC peripheral blood dataset was drawn from GSE31682, consisting of 20 healthy volunteers and 48 individuals with OC. After omitting samples lacking adequate follow-up [16], RNA-seq measurements were gathered from TCGA [17] and ICGC. Additionally, GEO datasets processed on the GPL570 array platform (n = 597)—specifically GSE19829, GSE18520, GSE9891, GSE26193, GSE30161, and GSE63885—were included. ICGA and TCGA sequencing files were merged to form a meta–RNA-seq resource, whereas GPL570 datasets were combined into a meta-microarray collection. Batch-related noise across these sources was addressed using the **"sva"** package.

Pre-processing of single-cell RNA sequencing data

Because human AMI single-cell datasets are limited, the mouse dataset GSE135310 was incorporated as a surrogate [15]. This dataset captures cardiac $CD45^+$ leukocyte profiles harvested from mice exposed to AMI or sham procedures at multiple stages. As no healthy, same-batch peripheral blood scRNA controls were available, we used paired chemotherapy-before/after samples instead. Two such samples from OC patients were taken from GSE213243. To ensure reliable scRNA quality, we kept cells expressing 200–2500 genes, excluding those with >10% mitochondrial content. Batch offsets were corrected using Harmony, and cluster identities were assigned with SingleR.

Clinical samples

Following our earlier work [15], peripheral blood mRNA confirmation was carried out in the same participant group. A total of ten early AMI and ten CAD patients were enrolled between January 2023 and March 2023. Blood was drawn shortly after symptom onset, prior to administration of anticoagulants or antiplatelet medication. PBMCs were purified using standard density-gradient protocols [18].

Immunohistochemical techniques and RT-qPCR

Immunohistochemistry (IHC) uses antigen-specific antibodies tagged with chromogenic or fluorescent labels, enabling direct visualization under microscopy. The IHC tissue sections used here originated from the Human

Protein Atlas. To confirm transcript expression, PBMC samples were used for AMI verification, and OC-related expression was tested using cell lines. The IOSE-80 (CP-H055) and SKOV3 (CL-0215) lines were obtained from Procell Life Science and Technology Co. Ltd. They were propagated in RPMI-1640 supplemented with 10% FBS and 1% penicillin/streptomycin, maintained at 37°C and 5% CO_2. Total RNA was isolated with the FastPure Cell/Tissue Total RNA Isolation Kit V2 (Vazyme). RT-qPCR was run on the LightCycler 480 II using HiScript III All-in-one RT SuperMix and ChamQ Universal SYBR qPCR Master Mix (Vazyme). Relative gene abundance was quantified via the $2^{-}\Delta\Delta Ct$ approach. Primers were chosen on the basis of published references and PrimerBank [19] for WEE1 [20], PYHIN1 [21], SEC61A2, and HAL [22].

CIBERSORT

CIBERSORT [23], which infers immune-cell composition from bulk transcriptomic profiles using a deconvolution-based support vector regression model, was applied to GSE59867, GSE31682, and the aggregated meta–RNA-seq sets (TCGA-OV and ICGC-OV). The method computes proportional contributions of each immune cell type using a predefined signature matrix.

Weighted gene co-expression network analysis

To explore coordinated transcriptional behavior, we applied Weighted Gene Co-expression Network Analysis (WGCNA) [24]. This method constructs networks by evaluating gene–gene correlation patterns across samples, allowing groups of co-expressed genes (modules) to be identified. Module–trait associations were examined using the monocyte scores generated by CIBERSORT, enabling us to pinpoint modules linked to specific biological features. The soft-thresholding powers chosen for network construction were $\beta = 7$ for OC, and $\beta = 9$ for AMI, and each resulting module was required to contain at least 50 genes.

Least absolute shrinkage and selection operator regression

A 10-fold cross-validation strategy was used to determine the optimal λ parameter. In this step, we aimed to select the λ that provided the best predictive penalty function, using AMI occurrence as the endpoint and sample-wise gene expression changes as input variables. For each tested λ, a LASSO model [25] was trained and then evaluated on a validation fold using performance measures such as the area under the curve or mean squared error. The λ producing the lowest validation error was deemed optimal. This enabled an extensive refinement of monocyte-related candidate diagnostic genes.

Establishment and validation of the logistic regression model

A logistic-regression–based nomogram was constructed to support risk estimation [26]. Coefficients for the four genes—WEE1, PYHIN1, SEC61A2, and HAL—were obtained from the fitted model, and these coefficients were converted into point scores. Summing the individual point contributions produced a subject-specific predicted probability. To assess the reliability of this model, we generated calibration plots, decision curve analysis (DCA) graphs, and clinical impact curves, using datasets GSE62646 and GSE59867 for external validation.

Establishment and validation of the Cox regression model

For survival analyses, we built a Cox proportional hazards model using the same four candidate genes. After selecting WEE1, PYHIN1, SEC61A2, and HAL as predictors, the Cox model was fit in the meta–RNA-seq datasets to estimate regression coefficients. Individual risk scores were computed using the formula: risk score = Σ (Expi × coefi), where each gene's coefficient and expression level contribute to the overall score. Model performance was then verified in the meta-microarray cohorts using calibration curves, ROC analyses, and log-rank tests to distinguish high- from low-risk groups.

Enrichment analysis

For pathway-level interpretation, we used the hallmark gene sets (h.all.v7.5.1.symbols.gmt) [27], which summarize major biological programs such as immunity, DNA repair, metabolism, and cell-cycle control. We implemented Gene Set Variation Analysis (GSVA) [28] to convert gene expression matrices into enrichment scores, producing sample-specific activity values for each hallmark pathway.

Statistical analysis

All statistical procedures were conducted in R version 4.1.2. Group differences were mainly assessed using the Wilcoxon rank-sum test. A p-value < 0.05 was regarded as statistically significant, with thresholds reported as *p < 0.05, **p < 0.01, and ***p < 0.001.

Results and Discussion

Monocytes as potential indicators for AMI prediction and cancer-related outcomes

Coronary artery disease (CAD) remains one of the leading contributors to global morbidity and mortality. Even individuals diagnosed with stable CAD retain a residual risk of developing acute myocardial infarction (AMI), a major and dangerous consequence of CAD. For this reason, CAD cohorts are frequently selected as comparison groups when examining blood-based immune alterations in AMI. In the present work, we initially assessed immune-cell composition using the CIBERSORT algorithm on a peripheral blood microarray dataset including both AMI and CAD samples. AMI cases showed reduced proportions of $CD8^+$ T lymphocytes, memory $CD4^+$ T cells, resting NK cells, and M2 macrophages, while displaying elevated levels of Tregs, inactive mast cells, neutrophils, and monocytes **(Figure 1a)**.

We then evaluated immune-cell shifts in ovarian cancer (OC) relative to healthy controls. Notably, only monocytes exhibited a directional change similar to that seen in AMI, implying a shared biological relevance **(Figure 1b)**. To reinforce these observations, we performed dimensionality-reduction analysis using single-cell datasets from sham and AMI subjects, producing six clearly separated clusters: monocytes, endothelial cells, macrophages, granulocytes, NK cells, and B cells **(Figure 1c)**. Following AMI onset, monocyte abundance increased, which aligned with the bulk-transcriptome findings.

Because same-batch healthy single-cell controls were unavailable, we utilized paired single-cell data taken before and after chemotherapy from the same OC patients. These profiles were grouped into four clusters **(Figure 1d)**, and a marked reduction in monocytes was detected after treatment. Thus, monocytes decreased when tumor burden diminished but increased when malignancy was present **(Figure 1e)**.

Recognizing pathology as a diagnostic gold standard in oncology, we reassessed monocyte prognostic value in the TCGA-OV cohort, using CD14 as a monocyte marker. Increased CD14 expression in tumor tissue corresponded to poorer overall survival, confirming monocytes as a negative prognostic indicator for OC.

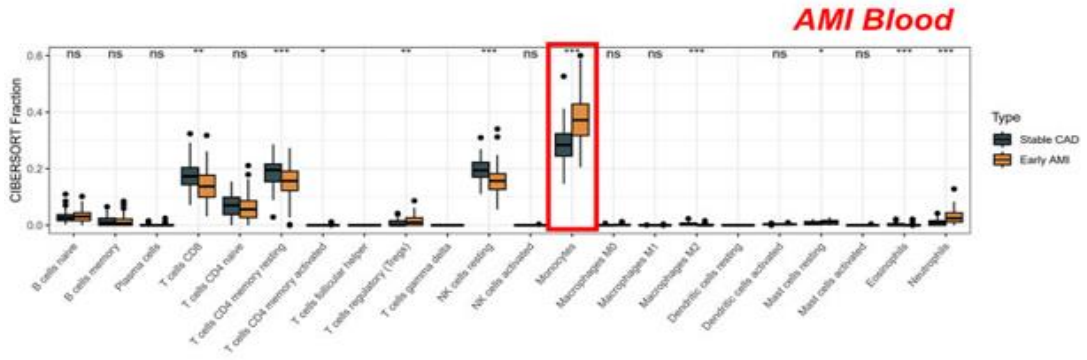

a)

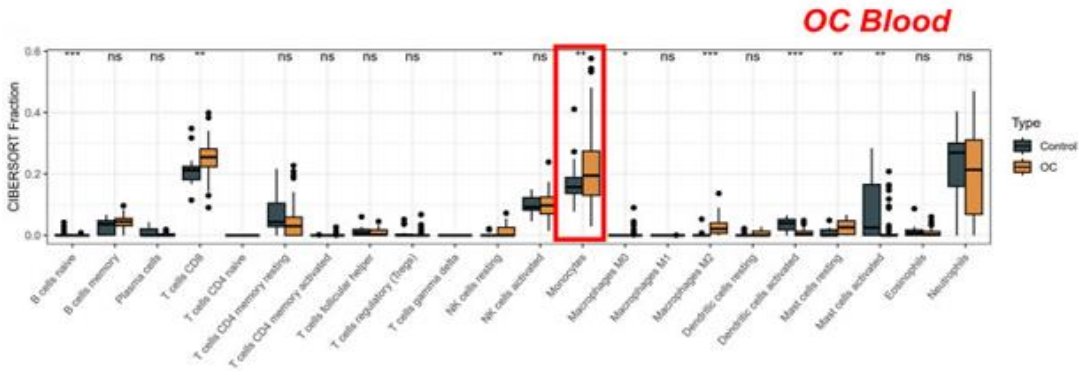

b)

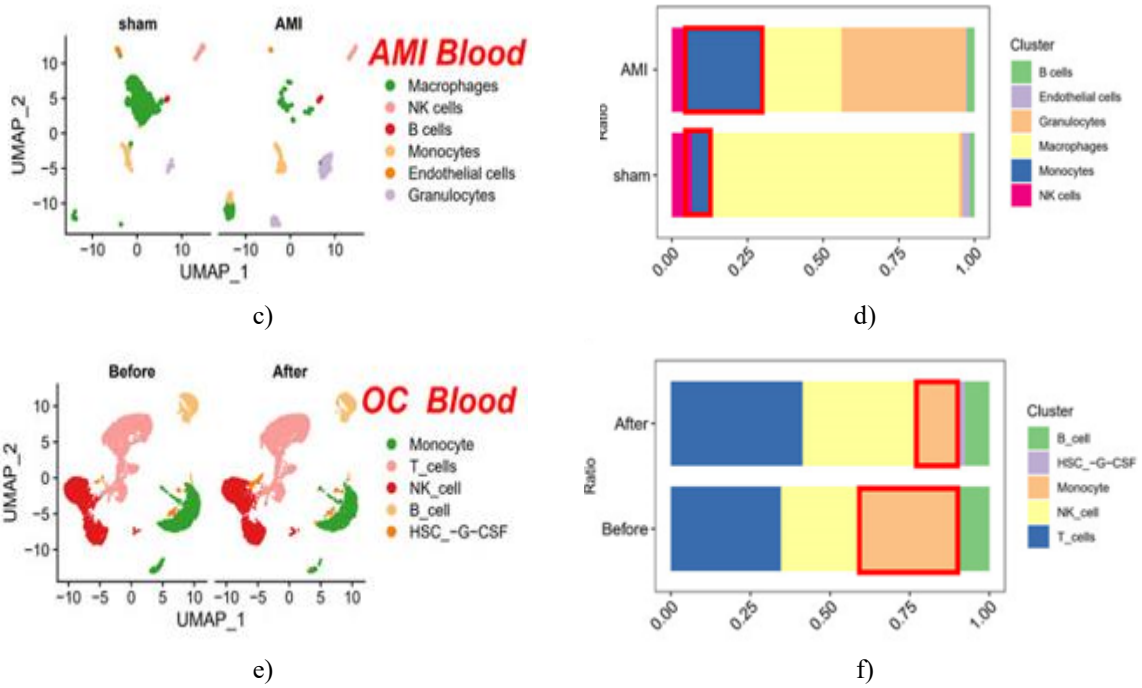

Figure 1. Comparison of immune-cell proportions in AMI vs. CAD and OC vs. normal groups. (a) CIBERSORT-based peripheral blood analysis for AMI and CAD. (b) CIBERSORT comparison in OC and healthy controls. (c) Single-cell dimensionality reduction in sham versus AMI. (d) Cell-proportion comparison in sham and AMI. (e) Dimensionality reduction in OC before and after chemotherapy. (f) Proportion shifts in OC pre- and post-treatment.

Biomarkers originating from monocytes identified through WGCNA in AMI and cancer

To refine the identification of monocyte-associated genes, we incorporated whole-transcriptome data into a weighted gene co-expression network analysis (WGCNA). Monocyte scores derived from CIBERSORT were treated as clinical traits to pinpoint modules most strongly linked to monocyte abundance. The optimal soft-thresholding powers were β = 7 for OC **(Figure 2a)** and β = 9 for AMI **(Figure 2b)**. Examination of module–trait correlations **(Figures 2c and 2d)** revealed that, in OC datasets, the purple and brown modules had the highest absolute correlation with monocyte scores **(Figure 2e)**, while in AMI datasets, the strongest associations occurred in the purple and yellow modules **(Figure 2f)**. These four modules were selected as key modules, from which 23 intersecting genes were extracted **(Figure 2g)**.

Next, we applied the LASSO method to the AMI dataset to further narrow down these 23 genes. Using AMI occurrence as the endpoint and gene-expression variation as predictors, we calculated the optimal λ **(Figures 2h and 2i)**. This procedure yielded seven genes—HRH4, LTBR, WEE1, HAL, PYHIN1, S100A12, SEC61A2.

Using OC RNA-seq data, we tested the prognostic significance of these candidates. Three genes—WEE1, PYHIN1, and SEC61A2—were linked to poorer outcomes, whereas HAL was associated with improved survival.

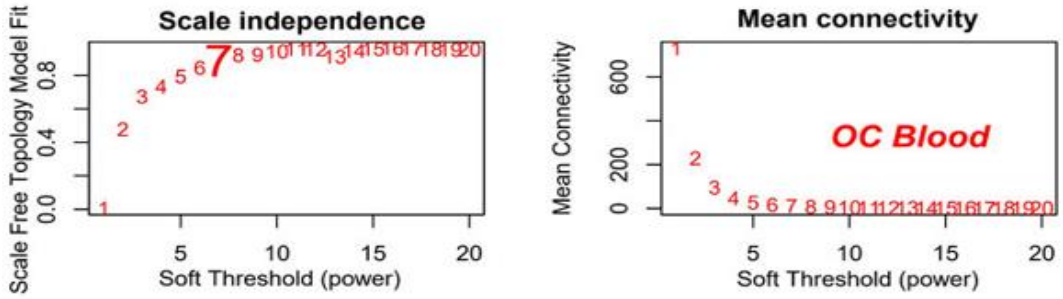

a)

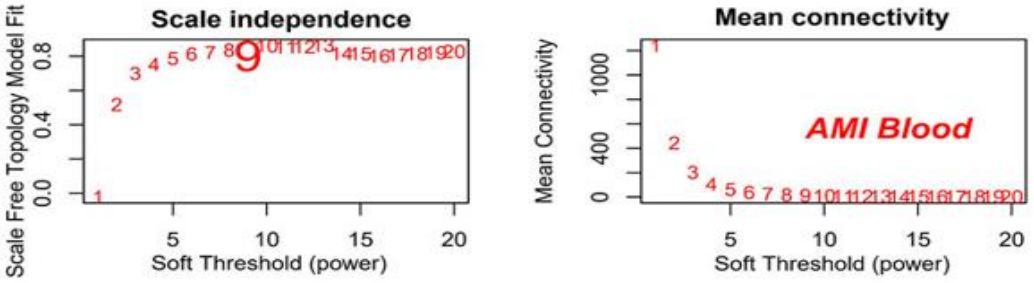
Scale independence
Scale Free Topology Model Fit
Soft Threshold (power)
Mean connectivity
Mean Connectivity
AMI Blood
Soft Threshold (power)

b)

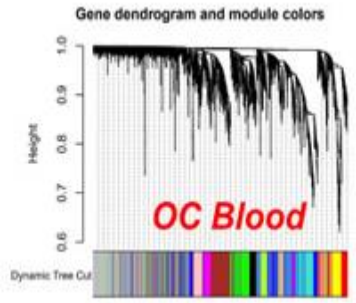
Gene dendrogram and module colors
Height
OC Blood
Dynamic Tree Cut

c)

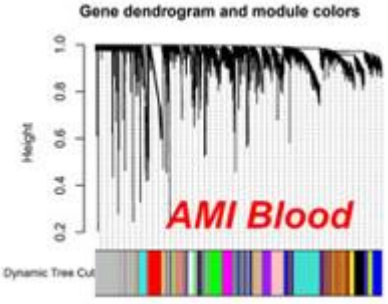
Gene dendrogram and module colors
Height
AMI Blood
Dynamic Tree Cut

d)

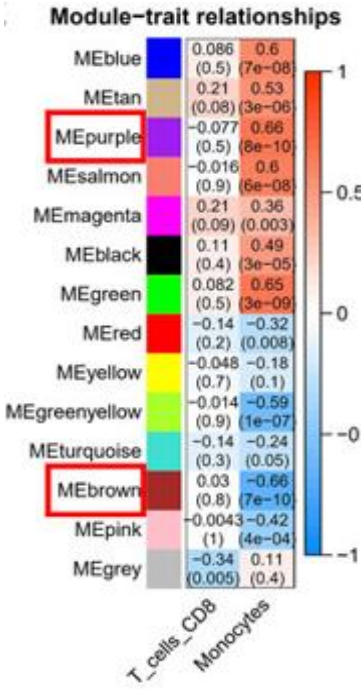
Module−trait relationships
MEblue
MEtan
MEpurple
MEsalmon
MEmagenta
MEblack
MEgreen
MEred
MEyellow
MEgreenyellow
MEturquoise
MEbrown
MEpink
MEgrey
T_cells_CD8
Monocytes

e)

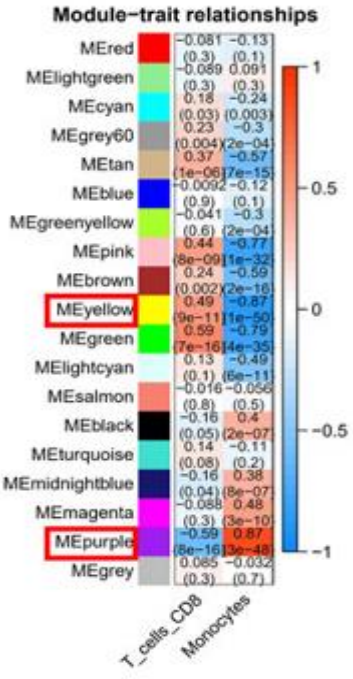
Module−trait relationships
MEred
MElightgreen
MEcyan
MEgrey60
MEtan
MEblue
MEgreenyellow
MEpink
MEbrown
MEyellow
MEgreen
MElightcyan
MEsalmon
MEblack
MEturquoise
MEmidnightblue
MEmagenta
MEpurple
MEgrey
T_cells_CD8
Monocytes

f)

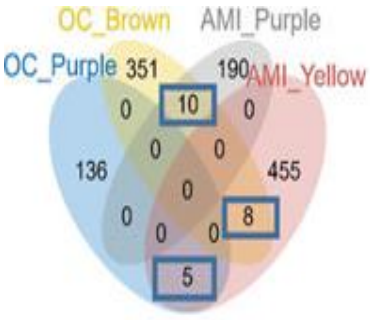
OC_Brown
AMI_Purple
OC_Purple
351
190
AMI_Yellow
10
136
455
8
5

g)

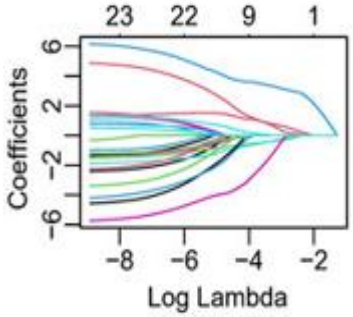
23
22
9
1
Coefficients
Log Lambda

h)

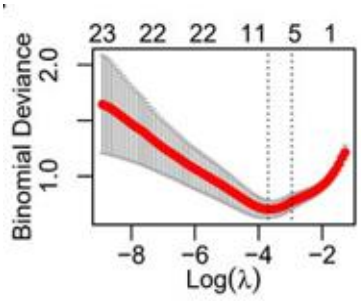

i)

Figure 2. WGCNA-based identification of monocyte-related signatures. (a) Soft-threshold selection (β) for OC. (b) Soft-threshold selection (β) for AMI. (c–d) Cluster dendrograms and module assignments for OC and AMI. (e–f) Module–trait correlations for monocyte scores in OC and AMI. (g) Venn diagram showing gene overlap. (h) Lambda selection for LASSO. (i) LASSO coefficient profiles.

Summary

Collectively, these results indicate that WEE1, PYHIN1, SEC61A2, and HAL, derived from monocyte-associated modules, may be valuable predictors of AMI occurrence and cancer prognosis.

Establishment of the monocyte-associated diagnostic signature in AMI

Within the AMI dataset, several key findings emerged. WEE1 (p = 2.4e-11) showed pronounced downregulation and delivered strong diagnostic accuracy, achieving an AUC of 0.839 (95% CI: 0.768–0.899), as displayed in **Figure 3a**. Likewise, both PYHIN1 **(Figure 3b)** and SEC61A2 **(Figure 3c)** were significantly reduced in AMI samples and produced reliable diagnostic discrimination, with AUCs of 0.782 and 0.747, respectively. In contrast, HAL was notably upregulated in AMI and yielded an AUC of 0.766 **(Figure 3d)**.

To improve the predictive performance and clinical usability of these markers, we constructed a nomogram incorporating the four genes mentioned above **(Figure 3e)**. The calibration curve confirmed that the nomogram performed accurately and consistently in distinguishing AMI from CAD **(Figure 3f)**. Further support came from the DCA curve **(Figure 3g)** and the clinical impact curve **(Figure 3h)**, both indicating strong diagnostic benefit. In the external validation dataset (GSE62646), the calibration plot **(Figure 3i)**, DCA analysis **(Figure 3j)**, and clinical impact curve **(Figure 3k)** collectively reaffirmed the nomogram's excellent generalizability.

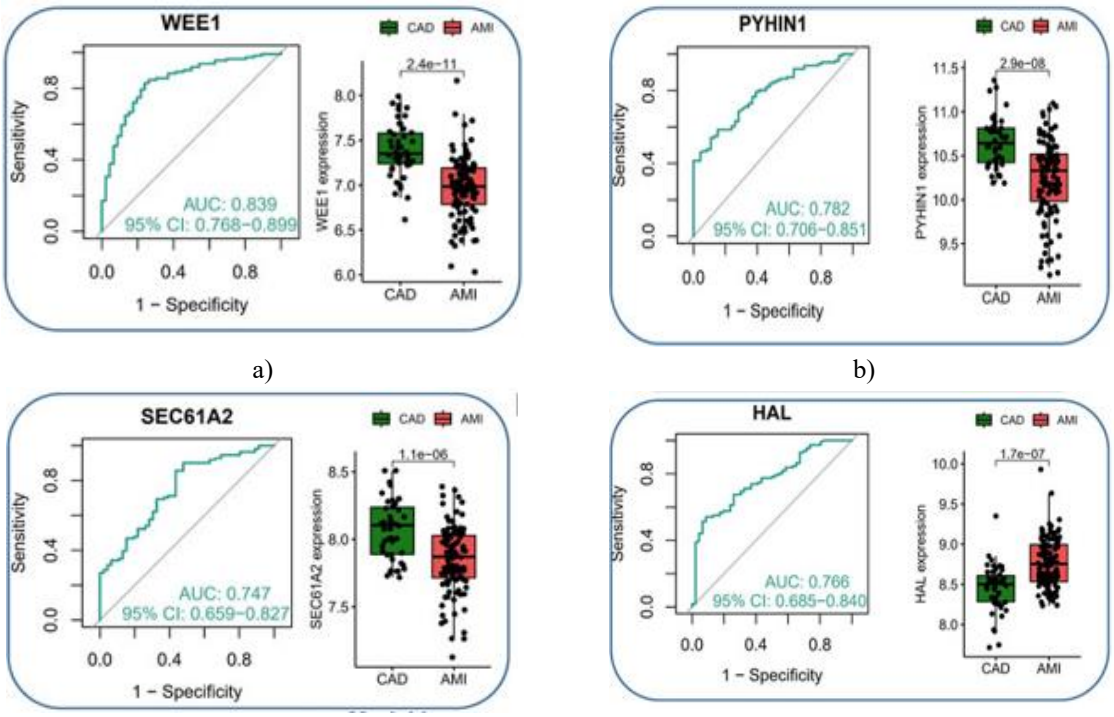

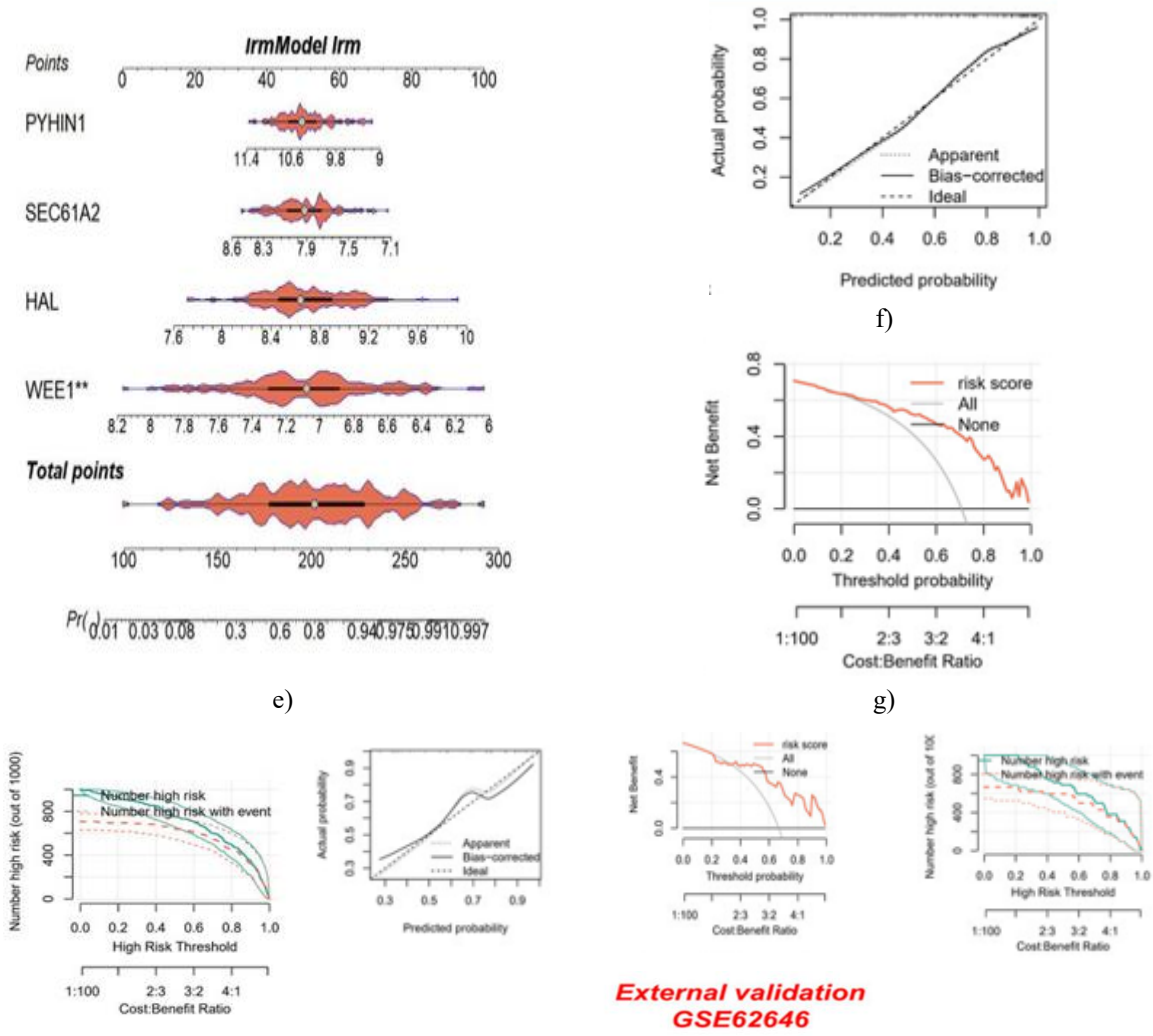

e) f) g) h) i) j) k)

Figure 3. Diagnostic evaluation of the AMI nomogram. (a–d) ROC curves and expression boxplots for WEE1, PYHIN1, SEC61A2, and HAL. (e) Nomogram integrating all four genes. (f) Calibration assessment in CAD subjects. (g–h) DCA and clinical impact curves. (i–k) External validation via calibration, DCA, and clinical impact analyses.

Establishment of the monocyte-associated prognostic signature in cancer

Given that tumor therapy relies heavily on surgical tissue acquisition, we examined expression patterns of the four selected genes across multiple tissue types using both the GTEx and HPA datasets. For WEE1, elevated expression was observed in tumor tissue at both protein and mRNA levels **(Figure 4a)**. PYHIN1 also showed significantly higher mRNA abundance in cancer samples, although protein staining was not apparent **(Figure 4b)**. HAL, in contrast, did not differ markedly in mRNA content between tissue types, yet demonstrated protein upregulation in tumors **(Figure 4c)**. Although SEC61A2 lacked an available IHC antibody, structural analysis and expression data indicated strong mRNA overexpression in normal tissues **(Figure 4d)**.

To estimate individual survival risk in ovarian cancer, we built a multivariable Cox model **(Figure 4d)** based on WEE1, PYHIN1, SEC61A2, and HAL. The resulting equation was:

$$\text{Risk score} = (-0.195 \times \text{WEE1}) + (-0.335 \times \text{PYHIN1}) + (-0.191 \times \text{SEC61A2}) + (0.137 \times \text{HAL}). \quad (1)$$

Gene-specific survival plots revealed that PYHIN1, SEC61A2, and WEE1 acted as protective factors, where lower expression appeared to correspond with extended survival **(Figure 4f)**. Conversely, HAL represented a risk-enhancing factor, with higher expression linked to poorer outcomes.

Correlation analysis demonstrated predominantly negative inter-gene associations **(Figure 4g)**. HAL correlated negatively with WEE1 and PYHIN1, but positively with SEC61A2. For overall risk scoring, only HAL showed a significant positive relationship ($R = 0.442$, $p < 0.001$).

Applying the Cox-derived formula to both the meta-RNA-seq and meta-microarray cohorts produced patient-specific risk values. Subjects were separated into high- and low-risk groups using the median score. In the meta-RNA-seq cohort, the high-risk group experienced significantly poorer overall survival **(Figure 5a)**, and the same pattern was observed in the meta-microarray set **(Figure 5b)**.

To evaluate long-term predictive accuracy, we examined ROC curves for 1-, 3-, 5-, and 10-year OS. In the training (meta-RNA-seq) cohort, the AUCs were 0.728, 0.692, 0.673, and 0.708, respectively **(Figure 5c)**. The validation (meta-microarray) cohort produced corresponding AUCs of 0.595, 0.578, 0.625, and 0.697 **(Figure 5d)**.

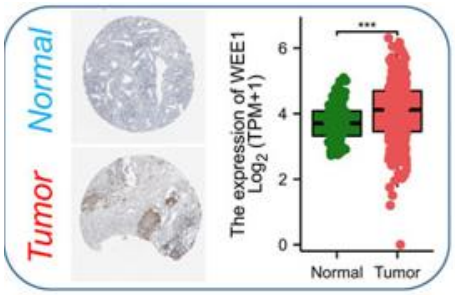

a)

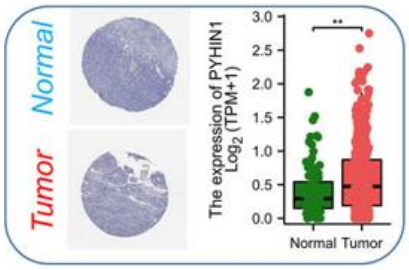

b)

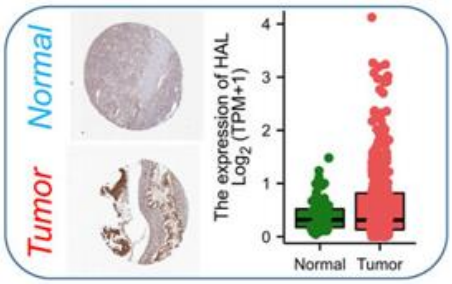

c)

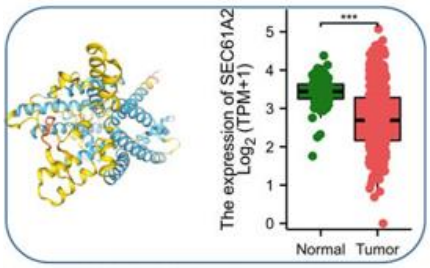

d)

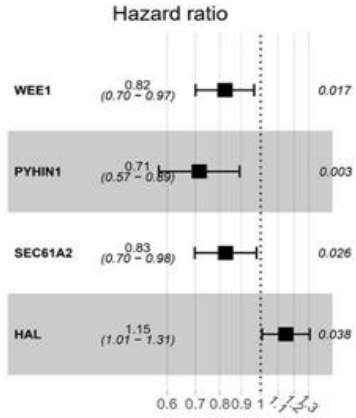

e)

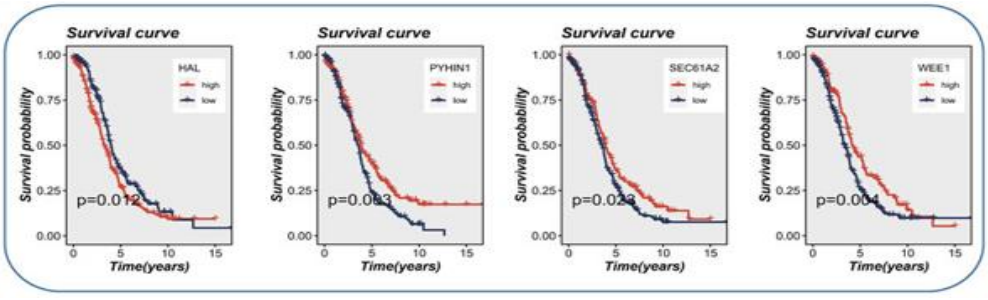

f)

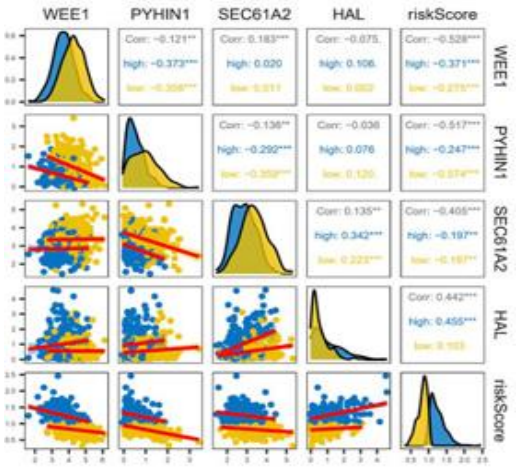

g)

Figure 4. Gene Expression Profiling and Construction of the Prognostic Framework.
(a) Protein and transcript abundance of WEE1 across sample categories.
(b) Protein and transcript abundance of PYHIN1 in the analyzed specimens.
(c) Protein and transcript levels of HAL in multiple sample types.
(d) mRNA expression patterns and structural depiction of SEC61A2.
(e) Assembly of a multi-gene Cox risk model incorporating WEE1, PYHIN1, SEC61A2, and HAL.
(f) Overall survival curves showing the individual prognostic contribution of each gene.
(g) Correlation matrix demonstrating the relationships among the four model genes.

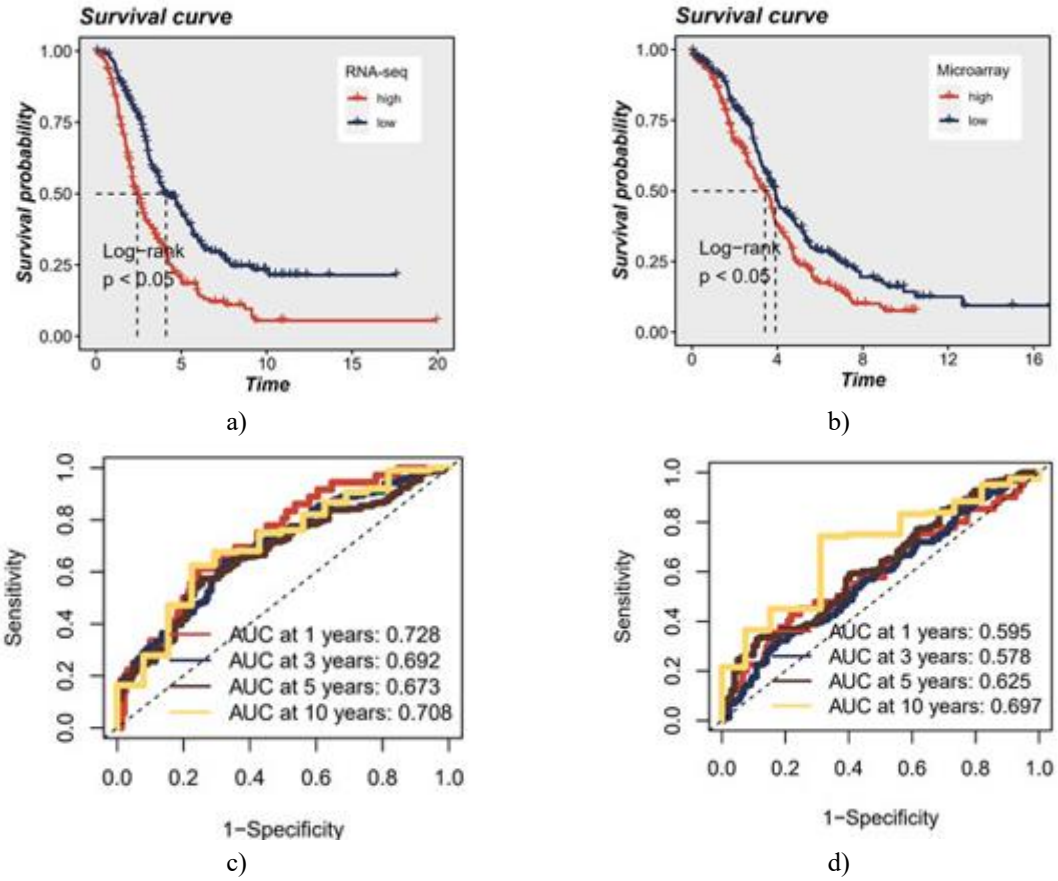

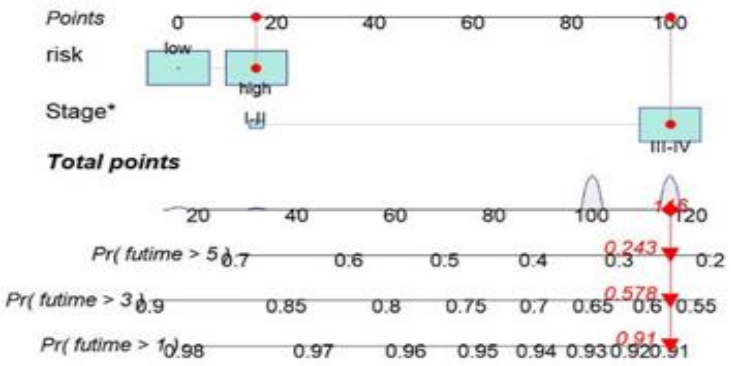

e)

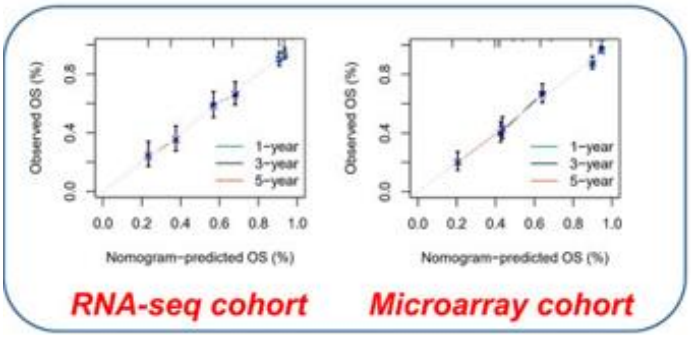

f)

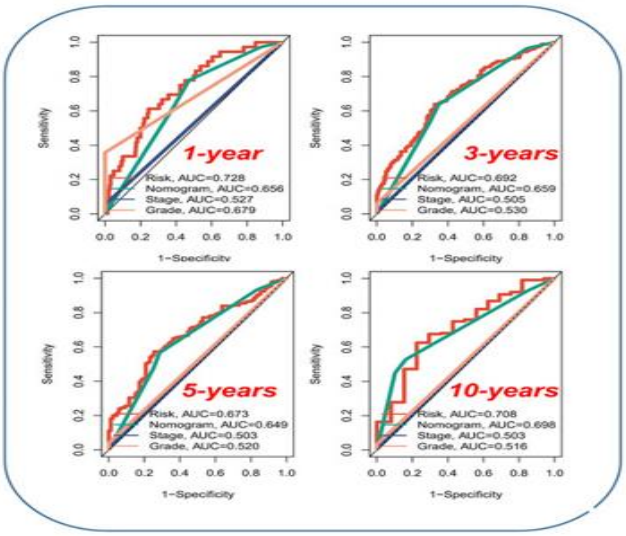

g)

Figure 5. Prognostic Assessment and Nomogram Performance.
(a) Kaplan–Meier curves for the meta–RNA-seq dataset.
(b) Kaplan–Meier survival comparison in the meta–microarray dataset.
(c) ROC curves for 1-, 3-, 5-, and 10-year survival prediction in the meta–RNA-seq cohort.
(d) ROC curves for 1-, 3-, 5-, and 10-year survival prediction in the meta–microarray cohort.
(e) A clinical nomogram integrating FIGO stage and calculated risk score for evaluating ovarian cancer prognosis.
(f) Calibration plots demonstrating nomogram accuracy in both meta–RNA-seq and meta–microarray datasets.
(g) ROC comparison of the nomogram versus other clinical indicators and existing score systems.

To maintain consistency with the AMI diagnostic framework, a graphical nomogram incorporating FIGO staging and the calculated risk level was applied to estimate patient outcomes **(Figure 5e)**. Calibration analyses indicated

that its predictive reliability was high in both cohorts **(Figure 5f)**. Moreover, ROC evaluations showed that the nomogram surpassed other clinical predictors for early survival, whereas for long-term outcomes (>5 years), the isolated risk-score model performed more effectively **(Figure 5g)**.

Immune cell infiltration in AMI and cancer

CIBERSORT was employed to profile immune cell distributions in high- and low-risk categories and to examine how these patterns aligned with model genes. Notably, the high-risk subgroup demonstrated reduced CD8+ T cells and lower M1 macrophage abundance **(Figure 6a)**. CD8+ T cells function as cytotoxic responders [29], while M1 macrophages release pro-inflammatory mediators [30]; their decline suggests an immunologically "cold" microenvironment.

A substantial positive association was detected between PYHIN1 expression and CD8+ T-cell abundance, implying that PYHIN1 may modulate cytotoxic T-cell dynamics **(Figure 6b)**. Risk-score distribution patterns also showed inverse correlations between CD8+ T cells and risk level, with noticeable shifts among M0/M1/M2 macrophage proportions.

Parallel analyses in AMI samples revealed similar findings: PYHIN1 expression correlated strongly and positively with CD8+ T cells and may influence the expansion of resting NK cells **(Figure 6c)**.

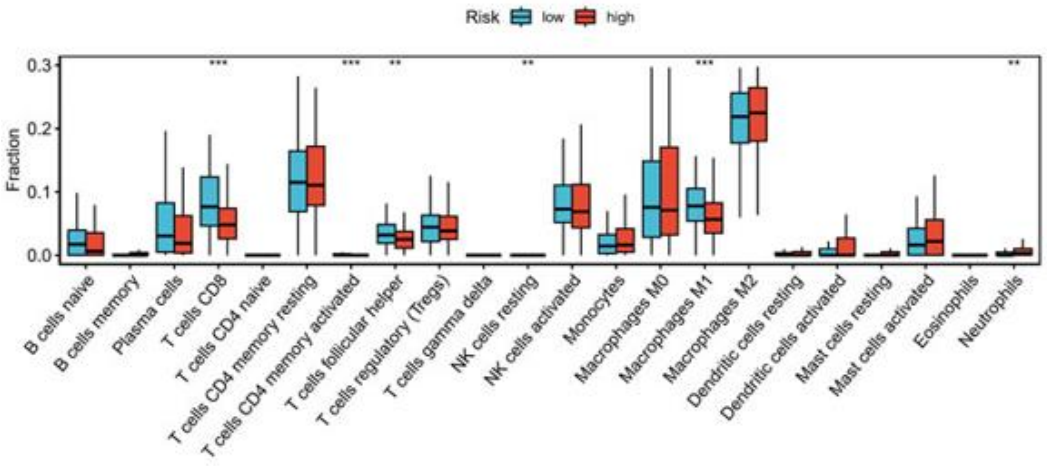

a)

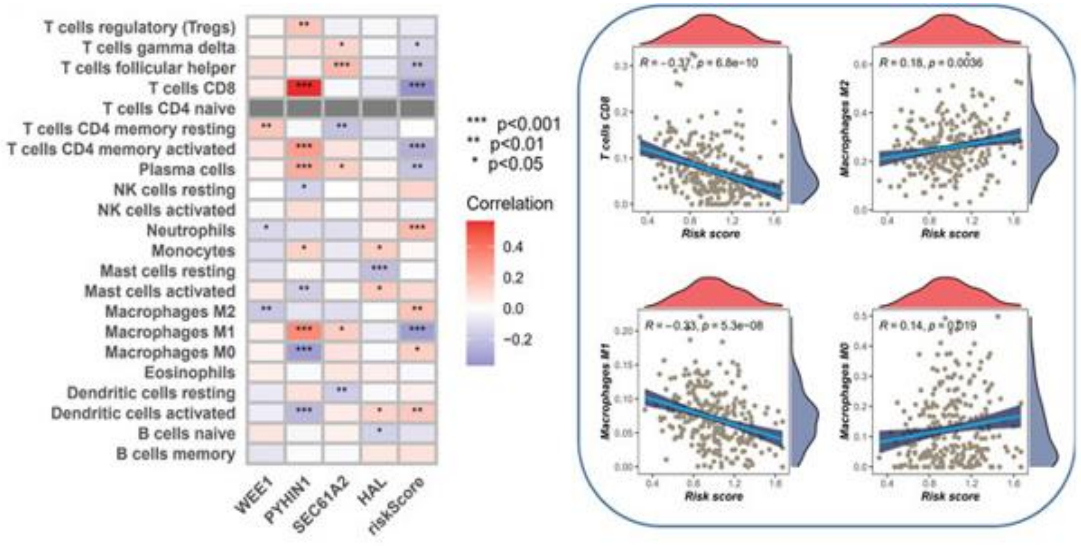

b)

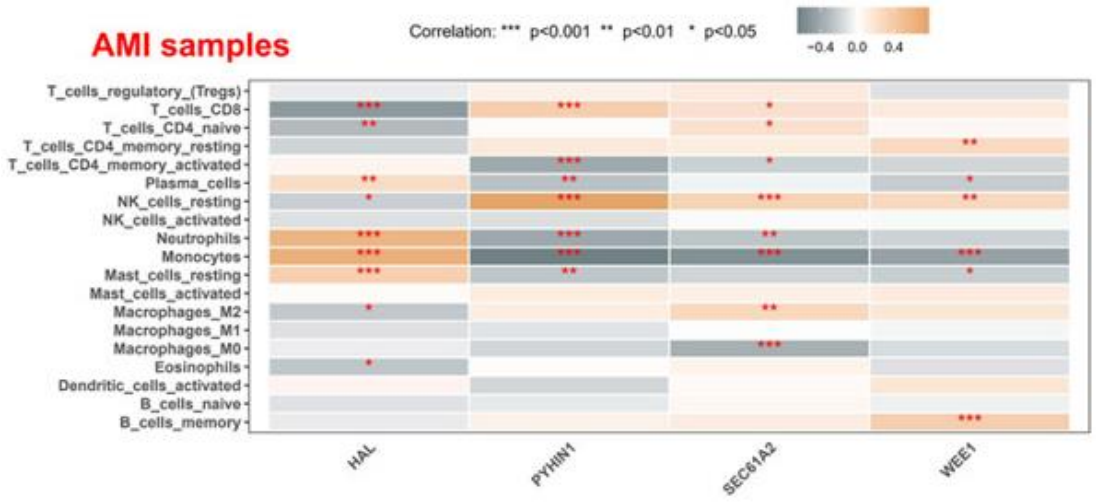

c)

Figure 6. Immune Microenvironment and Gene Associations.
(a) CIBERSORT-based immune cell profiling in high- and low-risk samples.
(b) Associations between immune cells and model-gene expression.
(c) Correlation analysis of model genes with immune-cell subsets in AMI.

Enrichment analysis

GSVA of hallmark pathways revealed distinct functional signatures between risk groups in ovarian cancer. In the high-risk category, top enriched pathways included Estrogen Response Early, Myogenesis, Notch Signaling, Bile Acid Metabolism, and Heme Metabolism **(Figure 7a)**. In the low-risk group, the most enriched pathways were E2F Targets, G2M Checkpoint, PI3K/AKT/MTOR Signaling, MYC Targets V1, and Mitotic Spindle.

We also assessed pathway alterations between AMI and CAD subjects, identifying pronounced activation of the P53 Pathway, Hypoxia, and Notch Signaling in AMI **(Figure 7b)**. The shared activation of Notch Signaling may highlight a mechanistic link contributing to elevated risk in both cancer and AMI.

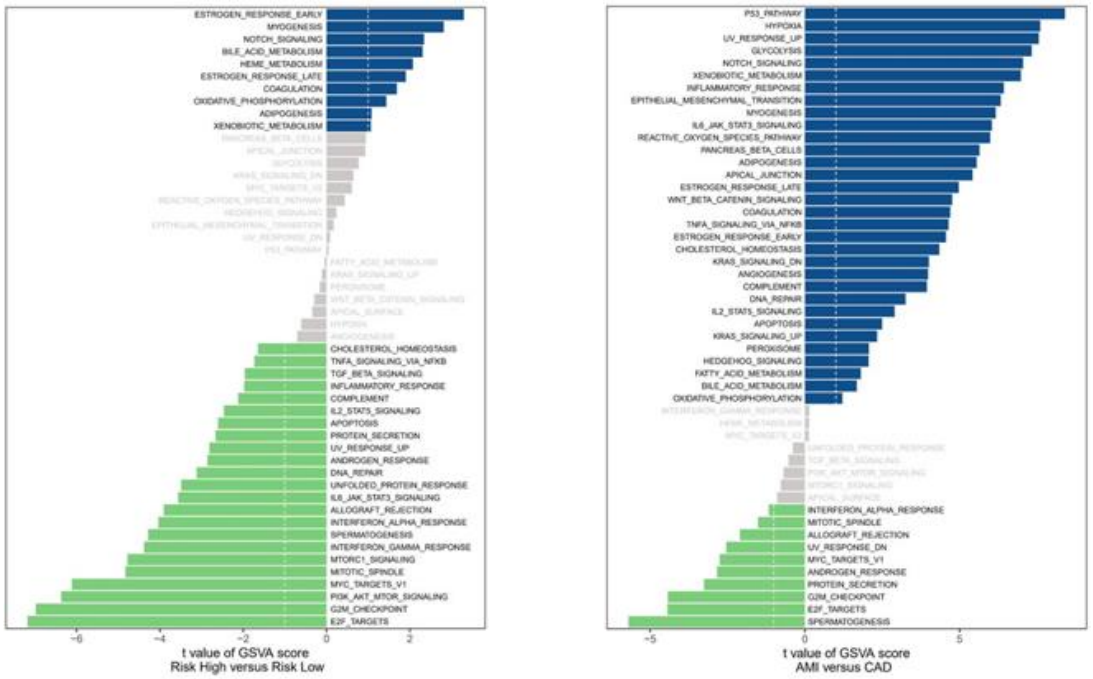

a) b)

Figure 7. Pathway Enrichment Findings.
(a) GSVA-derived pathway distinctions in ovarian cancer samples.
(b) GSVA-based pathway activity differences between AMI and CAD cases.

Validation of mRNA expression in clinical samples

To confirm the stability of the four prognostic markers, qRT-PCR assays were conducted on patient-derived PBMCs and cell lines. In PBMCs, gene-expression trends matched microarray findings **(Figures 3a–3d)**: WEE1, PYHIN1, and SEC61A2 were reduced in AMI versus CAD, whereas HAL was elevated.

Similarly, cell-line validation aligned with RNA-seq results. When compared with IOSE-80 cells, SKOV3 displayed higher expression of WEE1, PYHIN1, and HAL, while SEC61A2 was decreased.

Acute myocardial infarction (AMI) and cancer are globally widespread, life-threatening disorders that heavily impact health systems [2]. Although each condition has been examined extensively on its own, the biological and clinical links between the two remain insufficiently explored. Identifying shared molecular indicators could help pinpoint individuals susceptible to either disease, allowing clinicians to tailor preventive care. Stratifying patients according to their molecular risk may support more personalized recommendations, including lifestyle guidance, pharmacological strategies, and planned monitoring, while also reducing diagnostic burden by relying on overlapping biomarkers rather than multiple independent tests.

In this work, we observed that monocyte-derived genes—WEE1, PYHIN1, SEC61A2, and HAL—may function as predictors for both AMI and cancer outcomes. WEE1, a cell-cycle–associated kinase central to DNA damage control, maintains genomic integrity [31, 32]. Elevated WEE1 activity has been documented in many malignancies, promoting tumor progression, drug resistance, and unfavorable prognosis. Mohamed *et al*. (2018) [33] showed that cardiomyocytes overexpressing cyclin-dependent kinase proteins (CDK1, CDK4) and cyclins B1/D1 can undergo sustained division, enabling pronounced cardiac regeneration after myocardial infarction. They further demonstrated that blocking Wee1 together with Tgf-β reduced the dependence on CDK1 and cyclin B, underscoring WEE1's importance in regulating cardiomyocyte renewal. Chen and Gardner (2004) [34] reported that endothelin stimulates the proliferation of rat aortic smooth muscle cells by enhancing CDK2 and CDC2 through MEK/ERK/RSK signaling, while simultaneously inactivating WEE1 and increasing CDC25A, reinforcing WEE1's role in endothelin-mediated mitogenic activity.

PYHIN1, belonging to the PYHIN protein family, exhibits tumor-suppressive or tumor-promoting properties depending on cancer type [9, 10, 35]. Its functions include participation in DNA repair, cell-cycle dynamics, immune modulation, and inflammatory pathways. In a study of blood pressure responses in African Americans (AA) and European Americans (EA), de Las Fuentes *et al*. (2013) [36] identified candidate loci associated with systolic pressure in AA—including NUDT12, CHL1, GRIA1, CACNB2, and PYHIN1—and ID3 for diastolic pressure in AA, indicating a potential influence of PYHIN1 on antihypertensive drug response, though none achieved genome-wide significance due to the limited sample size. Larger, ethnically diverse investigations are required.

SEC61A2, a component of the SEC61 translocation complex, is essential for protein movement across the endoplasmic reticulum membrane [37]. Vendrov *et al*. (2006) [38] examined NAD(P)H oxidase–dependent pathways in atherosclerosis and found that thrombin-induced NAD(P)H oxidase activity regulated several genes in vascular smooth muscle cells, including SEC61A2. Their results linked oxidase-mediated control of CD44 and BMP4-Id signaling to restenosis and plaque development, suggesting SEC61A2 may participate in vascular remodeling.

HAL (histidine ammonia-lyase) governs histidine degradation and affects histidine-related immune and angiogenic processes [39]. Blaeschke *et al*. (2019) [40], studying pediatric medulloblastoma, identified patient-specific immunogenic peptides—including HAL-derived epitopes—despite the tumor's low mutational burden, highlighting the feasibility of neoantigen-based T-cell therapies. Yu *et al*. (2015) [41] identified three rare loss-of-function variants in HAL that significantly modified blood histidine concentrations. Elevated histidine levels were linked to reduced coronary heart disease risk in both African Americans and European Americans, implying a cardioprotective role.

Recognizing these four genes as shared indicators for AMI and cancer prognosis offers insight into overlapping molecular pathways driving both conditions. Nonetheless, additional mechanistic and functional studies are essential to clarify how WEE1, PYHIN1, SEC61A2, and HAL contribute to disease initiation, progression, and therapeutic responsiveness in cancer and AMI.

We further employed a new computational approach to evaluate mRNA expression in clinical specimens from both a meta-RNA-seq dataset and a meta-microarray dataset. This approach generated an updated risk score derived from gene expression patterns. Using the median value of this score, participants were separated into high- and low-risk subgroups. Kaplan–Meier curves showed that individuals in the high-risk category had markedly

reduced overall survival in both cohorts. These results highlight the value of shared molecular indicators for forecasting cancer outcomes. Additionally, ROC analyses were conducted to measure predictive accuracy at multiple survival intervals. In the meta-RNA-seq training cohort, the AUC values showed moderate–good performance for 1-, 3-, 5-, and 10-year survival estimates, and the meta-microarray validation cohort demonstrated comparable accuracy across the same time frames. To enhance clinical interpretability, we incorporated FIGO stage and risk grouping into a visual nomogram. A corresponding nomogram was similarly generated for AMI diagnosis. Its calibration plot confirmed strong agreement between predicted and observed AMI diagnoses among CAD patients, while the DCA and decision curve analyses further supported its diagnostic robustness. In the external dataset (GSE62646), the calibration, DCA, and clinical impact curves jointly confirmed that the nomogram maintained excellent validation performance.

Within the cancer setting, the relationship between the risk score and immune-related signals suggests that patients classified as high-risk exhibit more pronounced immune dysregulation, potentially influencing their responsiveness to immunotherapy. Immunotherapeutic strategies—especially checkpoint blockade—have transformed oncology by boosting immune-mediated tumor clearance. Thus, our observations imply that individuals with elevated risk scores could be better suited for such treatments, as their altered immune state may render them more receptive. Likewise, in AMI, the association between the risk score and immune features underscores the pivotal role of immune activity in myocardial damage and recovery. Targeting immune mechanisms—such as controlling inflammation or encouraging reparative pathways—could offer new therapeutic opportunities. Hence, defining how immune signatures align with risk scores may assist in creating targeted immune-modulating interventions for AMI.

One notable finding is the shared activation of the Notch signaling cascade, which may help explain common high-risk mechanisms underlying both AMI and cancer. Notch signaling has multifaceted oncogenic functions, contributing to angiogenesis, resistance to therapy, and epithelial–mesenchymal transition. Blocking this pathway has become a promising anticancer strategy, and Notch inhibitors have shown potential in diminishing tumor aggressiveness [42, 43]. Yu *et al*. (2023) [43] also explored Notch signaling in innate lymphoid cells (ILCs) in acute coronary syndrome and observed that pathway activation shifted circulating ILCs from ILC1 toward ILC2 in AMI patients. Notch inhibition reversed this shift, increasing ILC1 levels and interferon-γ while reducing ILC2 levels and IL-5/IL-13, pointing to a regulatory role for Notch in AMI-associated ILC dynamics. Liu *et al*. (2019) [44] examined miR-29b in a rat myocardial infarction model and found that its downregulation corresponded with elevated Notch1, Dll4, Hes1, and NICD1, indicating that miR-29b mitigates fibrosis and hypertrophy via activating the Notch pathway. Matsuda *et al*. (2014) [45] evaluated how Notch modulation affects human cardiac stem cells (CSCs) and their therapeutic benefit in an AMI rat model, discovering that lowering Notch activity through low-density culture improved CSC proliferation, differentiation potential, and treatment effectiveness—emphasizing the importance of optimizing Notch-related culture conditions in regenerative cardiac therapy.

Clinical implications of the shared signature

The common signature identified in this study has practical relevance in guiding treatment strategies. Profiling these shared biomarkers in individual patients allows clinicians to stratify patients more precisely and anticipate their responsiveness to specific therapies. For instance, cancer or AMI patients exhibiting abnormalities in immune-related signature genes might respond more effectively to immunotherapy or treatments that modulate immune activity. Such information can inform therapy selection and enhance the implementation of precision medicine approaches.

Beyond treatment guidance, the common signature can also inform drug development. Targeting the shared dysregulated pathways revealed by these biomarkers offers opportunities for designing novel therapeutics or repurposing existing drugs to address both cancer and AMI. This approach may facilitate combination therapies that simultaneously correct these shared pathway abnormalities, potentially improving clinical outcomes. Additionally, assessing the expression or activation of these genes may support prognosis and risk stratification. Evaluating the common signature can help predict disease progression, recurrence, or complications, allowing clinicians to tailor monitoring and follow-up strategies for higher-risk patients.

Study limitations

Several limitations warrant consideration. The sample size for mRNA analyses was not explicitly reported, which may limit statistical robustness and generalizability. The study focused on monocyte-derived biomarkers,

potentially overlooking other relevant molecular indicators. Moreover, the retrospective design may introduce biases and limit the ability to infer causality. Prospective validation in larger and more diverse patient populations is necessary. Finally, while Notch signaling activation was highlighted as a shared mechanism, the precise molecular interactions connecting these biomarkers to AMI and cancer outcomes remain unclear. Future research should clarify these mechanistic links to strengthen the biological understanding of the shared signature.

Conclusion

In conclusion, identifying biomarkers common to cancer prognosis and AMI risk represents a crucial step toward improved patient care. Elucidating the underlying molecular mechanisms and integrating personalized preventive strategies could reduce disease burden and improve clinical outcomes. This study demonstrates the potential of mRNA-based biomarkers and underscores the importance of additional research to validate and refine these findings.

Acknowledgments: None

Conflict of Interest: None

Financial Support: None

Ethics Statement: None

References

1. Psaty BM, Vasan RS. The association of myocardial infarction with cancer incidence. Eur J Epidemiol. 2023;38(8):851–2. doi:10.1007/s10654-023-01019-y
2. Rinde LB, Smabrekke B, Hald EM, Brodin EE, Njølstad I, Mathiesen EB, et al. Myocardial infarction and future risk of cancer in the general population: the Tromsø Study. Eur J Epidemiol. 2017;32(3):193–201. doi:10.1007/s10654-017-0231-5
3. Leening MJG, Bouwer NI, Ikram MA, Kavousi M, Ruiter R, Boersma E, et al. Risk of cancer after ST-segment-elevation myocardial infarction. Eur J Epidemiol. 2023;38(8):853–8. doi:10.1007/s10654-023-00984-8
4. Howard E, Steingart RM, Armstrong GT, Lyon AR, Armenian SH, Voso MT, et al. Cardiovascular events in cancer survivors. Semin Oncol. 2019;46(5):426–32. doi:10.1053/j.seminoncol.2019.01.007
5. Shaikh AY, Shih JA. Chemotherapy-induced cardiotoxicity. Curr Heart Fail Rep. 2012;9(2):117–27. doi:10.1007/s11897-012-0083-y
6. Libby P, Kobold S. Inflammation: a common contributor to cancer, aging, and cardiovascular diseases: expanding the concept of cardio-oncology. Cardiovasc Res. 2019;115(5):824–9. doi:10.1093/cvr/cvz058
7. Zhao S, Wu Y, Wei Y, Xu X, Zheng J. Identification of biomarkers associated with CD8+ T cells in coronary artery disease and their pan-cancer analysis. Front Immunol. 2022;13:876616. doi:10.3389/fimmu.2022.876616
8. Wang Z, Gerstein M, Snyder M. RNA-seq: a revolutionary tool for transcriptomics. Nat Rev Genet. 2009;10(1):57–63. doi:10.1038/nrg2484
9. Ding JM, Lin WR, Fei ZD, Chen CB. PYHIN1 correlates with CD8+ T cell infiltration and confers good patient survival in oral cancer. J Dent Sci. 2022;17(1):551–9. doi:10.1016/j.jds.2021.06.014
10. Ding J, Sharon N, Bar-Joseph Z, Wu Z, Zhang X, Li B, et al. Recent advances in quantum dots-based biosensors for antibiotics detection. J Pharm Anal. 2022;12(3):355–64. doi:10.1016/j.jpha.2021.08.002
11. Reel PS, Reel S, Pearson E, Trucco E, Jefferson E. Using machine learning approaches for multi-omics data analysis: a review. Biotechnol Adv. 2021;49:107739. doi:10.1016/j.biotechadv.2021.107739
12. Stewart C, Ralyea C, Lockwood S. Ovarian cancer: an integrated review. Semin Oncol Nurs. 2019;35(2):151–6. doi:10.1016/j.soncn.2019.02.001
13. Kuhn F, Schiergens TS, Klar E. Acute mesenteric ischemia. Visc Med. 2020;36(4):256–62. doi:10.1159/000508739

14. Aydin S, Ugur K, Aydin S, Sahin I, Yardim M. Biomarkers in acute myocardial infarction: current perspectives. Vasc Health Risk Manag. 2019;15:1–10. doi:10.2147/VHRM.S166157
15. Pan HH, Yuan N, He LY, Sheng JL, Hu HL, Zhai CL. Machine learning-based mRNA signature in early acute myocardial infarction patients: the perspective toward immunological, predictive, and personalized. Funct Integr Genomics. 2023;23(2):160. doi:10.1007/s10142-023-01081-5
16. Feng S, Xu Y, Dai Z, Yin H, Zhang K, Shen Y. Integrative analysis from multicenter studies identifies a WGCNA-derived cancer-associated fibroblast signature for ovarian cancer. Front Immunol. 2022;13:951582. doi:10.3389/fimmu.2022.951582
17. Blum A, Wang P, Zenklusen JC. SnapShot: TCGA-analyzed tumors. Cell. 2018;173(2):530. doi:10.1016/j.cell.2018.03.059
18. Boyum A. Separation of leukocytes from blood and bone marrow: introduction. Scand J Clin Lab Invest Suppl. 1968;97:7.
19. Wang X, Spandidos A, Wang H, Seed B. PrimerBank: a PCR primer database for quantitative gene expression analysis, 2012 update. Nucleic Acids Res. 2012;40(D1):D1144–9. doi:10.1093/nar/gkr1013
20. Ma L, Lin Y, Sun SW, Xu J, Yu T, Chen WL, et al. KIAA1429 is a potential prognostic marker in colorectal cancer by promoting proliferation via downregulating WEE1 expression in an m6A-independent manner. Oncogene. 2022;41(5):692–703. doi:10.1038/s41388-021-02066-z
21. Lee YC, Chao YL, Chang CE, Hsieh MH, Liu KT, Chen HC, et al. Transcriptome changes in relation to manic episode. Front Psychiatry. 2019;10:280. doi:10.3389/fpsyt.2019.00280
22. Kozaczek M, Bottje W, Greene E, Lassiter K, Kong B, Dridi S, et al. Comparison of liver gene expression by RNA-seq and PCR after 8 weeks of feeding soy protein isolate- or casein-based diets in an obese liver steatosis rat model. Food Funct. 2019;10(12):8218–29. doi:10.1039/c9fo01387c
23. Chen B, Khodadoust MS, Liu CL, Newman AM, Alizadeh AA. Profiling tumor-infiltrating immune cells with CIBERSORT. Methods Mol Biol. 2018;1711:243–59. doi:10.1007/978-1-4939-7493-1_12
24. Langfelder P, Horvath S. WGCNA: an R package for weighted correlation network analysis. BMC Bioinformatics. 2008;9(1):559. doi:10.1186/1471-2105-9-559
25. Cheng X, Li J, Feng L, Feng S, Wu X, Li Y. Role of hypoxia-related genes in TACE-refractory hepatocellular carcinoma. Front Pharmacol. 2022;13:1011033. doi:10.3389/fphar.2022.1011033
26. Zhang K, Feng S, Ge Y, Ding B, Shen Y. Nomogram based on SEER database for predicting prognosis in mucinous ovarian cancer. Int J Womens Health. 2022;14:931–43. doi:10.2147/IJWH.S372328
27. Liberzon A, Birger C, Thorvaldsdottir H, Ghandi M, Mesirov JP, Tamayo P. The Molecular Signatures Database hallmark gene set collection. Cell Syst. 2015;1(6):417–25. doi:10.1016/j.cels.2015.12.004
28. Hanzelmann S, Castelo R, Guinney J. GSVA: gene set variation analysis for microarray and RNA-seq data. BMC Bioinformatics. 2013;14(1):7. doi:10.1186/1471-2105-14-7
29. Mittrucker HW, Visekruna A, Huber M. Heterogeneity in the differentiation and function of $CD8^+$ T cells. Arch Immunol Ther Exp (Warsz). 2014;62(6):449–58. doi:10.1007/s00005-014-0293-y
30. Mills CD, Lenz LL, Harris RA. A breakthrough: macrophage-directed cancer immunotherapy. Cancer Res. 2016;76(3):513–6. doi:10.1158/0008-5472.CAN-15-1737
31. Okabe S, Tanaka Y, Moriyama M, Gotoh A. WEE1 and PARP-1 play critical roles in myelodysplastic syndrome and acute myeloid leukemia treatment. Cancer Cell Int. 2023;23(1):128. doi:10.1186/s12935-023-02961-3
32. Su YL, Xiao LY, Huang SY, Wu CC, Chang LC, Chen YH, et al. Inhibiting WEE1 augments the antitumor efficacy of cisplatin in urothelial carcinoma. Cells. 2023;12(11):1471. doi:10.3390/cells12111471
33. Mohamed TMA, Ang YS, Radzinsky E, Zhou P, Huang Y, Elfenbein A, et al. Regulation of cell cycle to stimulate adult cardiomyocyte proliferation and cardiac regeneration. Cell. 2018;173(1):104–116.e12. doi:10.1016/j.cell.2018.02.014
34. Chen S, Gardner DG. Suppression of WEE1 and stimulation of CDC25A correlates with endothelin-dependent proliferation of rat aortic smooth muscle cells. J Biol Chem. 2004;279(14):13755–63. doi:10.1074/jbc.M310064200
35. Tong Y, Song Y, Deng S. Combined analysis and validation for DNA methylation and gene expression profiles associated with prostate cancer. Cancer Cell Int. 2019;19(1):50. doi:10.1186/s12935-019-0753-x

36. de Las Fuentes L, Sung YJ, Schwander KL, Kalathiveetil S, Hunt SC, Arnett DK, et al. Role of SNP-loop diuretic interactions in hypertension across ethnic groups in HyperGEN. Front Genet. 2013;4:304. doi:10.3389/fgene.2013.00304
37. Connerly PL, Esaki M, Montegna EA, Strongin DE, Levi S, Soderholm J, et al. Sec16 is a determinant of transitional ER organization. Curr Biol. 2005;15(15):1439–47. doi:10.1016/j.cub.2005.06.065
38. Vendrov AE, Madamanchi NR, Hakim ZS, Rojas M, Runge MS. Thrombin and NAD(P)H oxidase-mediated regulation of CD44 and BMP4-Id pathway in VSMC, restenosis, and atherosclerosis. Circ Res. 2006;98(10):1254–63. doi:10.1161/01.RES.0000221214.37803.79
39. Krzymuska A. Enzymes of histidine metabolism in normal and tumor tissues: histidase and urocanase activity. Arch Immunol Ther Exp (Warsz). 1964;12:724–9
40. Blaeschke F, Paul MC, Schuhmann MU, Rabsteyn A, Schroeder C, Casadei N, et al. Low mutational load in pediatric medulloblastoma still translates into neoantigens. Cytotherapy. 2019;21(9):973–86. doi:10.1016/j.jcyt.2019.06.009
41. Yu B, Li AH, Muzny D, Veeraraghavan N, de Vries PS, Bis JC, et al. Association of rare loss-of-function alleles in HAL, serum histidine levels, and incident coronary heart disease. Circ Cardiovasc Genet. 2015;8(2):351–5. doi:10.1161/CIRCGENETICS.114.000697
42. Sen P, Ghosh SS. Intricate notch signaling dynamics in therapeutic realms of cancer. ACS Pharmacol Transl Sci. 2023;6(5):651–70. doi:10.1021/acsptsci.2c00239
43. Yu H, Wei Y, Dong Y, Chen P. Regulation of notch signaling pathway to innate lymphoid cells in patients with acute myocardial infarction. Immunol Invest. 2023;52(2):241–55. doi:10.1080/08820139.2022.2158856
44. Liu Y, Wang H, Wang X, Xie G. MiR-29b inhibits ventricular remodeling by activating notch signaling pathway in rat myocardial infarction model. Heart Surg Forum. 2019;22(1):E019–23. doi:10.1532/hsf.2079
45. Matsuda T, Miyagawa S, Fukushima S, Kitagawa-Sakakida S, Akimaru H, Horii-Komatsu M, et al. Human cardiac stem cells with reduced notch signaling show enhanced therapeutic potential. Circ J. 2014;78(1):222–31. doi:10.1253/circj.cj-13-0534